Journal Name

COMMUNICATION

Colloidal nanocrystal deposition process: An advanced method to prepare high performance hematite photoanodes for water splitting

Ricardo H. Gonçalves, Edson R. Leite[*]

Much research has been devoted to improve the water splitting efficiency of hematite photoanodes. In this study, we are demonstrating a significant advance in the colloidal nanocrystal deposition (CND) process to obtain hematite thin films with a high photoelectrochemical performance. For this approach, we designed the magnetic field-assisted dip coating process to achieve homogeneous hematite thin films by using magnetic nanocrystals (maghemite) as the precursor. Using this non-aqueous deposition route, we produced undoped and Sn-doped hematite photoanodes with excellent photocurrents of 1.4 mA.cm^{-2} at 1.23 V$_{RHE}$ and 2.7 mA.cm^{-2} at 1.23 V$_{RHE}$, respectively, under a standard AM 1.5 G solar light simulator.

Decades ago, K.L Hardee and A.J. Bard researched hematite (α-Fe$_2$O$_3$) as a potential material for photoelectrochemistry devices due to its ability to absorb in visible light as well as its chemical stability in an alkaline medium and the abundance of this element.[1] The subsequent quest for direct solar-to-chemical conversion higher efficiency of the hematite photoanode was aggressively pursued. Hematite has a small optical absorption coefficient and poor electronic properties due to its short minority carrier (holes) diffusion lengths.[2-5] Despite this intrinsic disadvantage, many excellent research projects demonstrated good photoelectrochemical performance for hematite thin films,[6-11] which can be associated with morphological control at the nanoscale through a suitable thin film deposition process.

Among relevant deposition methods which were investigated to process hematite photoanodes, the atmospheric pressure chemical vapor deposition (APCVD) method is a benchmark with a photocurrent value of 2.2 mA.cm^{-2} at 1.23 V$_{RHE}$ without co-catalysis under standard air mass 1.5 illumination.[12] Atomic layer deposition (ALD) is also a powerful technique to produce high quality thin films[13]; e.g., nanonet-based hematite heterostructural growth by ALD achieved 1.6 mA.cm^{-2} at 1.23 V$_{RHE}$.[14] Another interesting

strategy is the growth of a hematite nanorod by hydrothermal and sintering processes that have been widely studied and show excellent photocurrent results.[15]

For the last three years, our research group has been working on a CND process to prepare hematite and other semiconductor oxide photoanodes with excellent activity for water splitting.[16] In this study, we demonstrate significant progress by using CND to prepare hematite thin films by introducing the following modifications in the original process as described in reference 16: a) the deposition of maghemite (γ-Fe$_2$O$_3$) instead of magnetite; b) the introduction of a magnetic field during the dip coating process; and c) the introduction of an intentional doping.
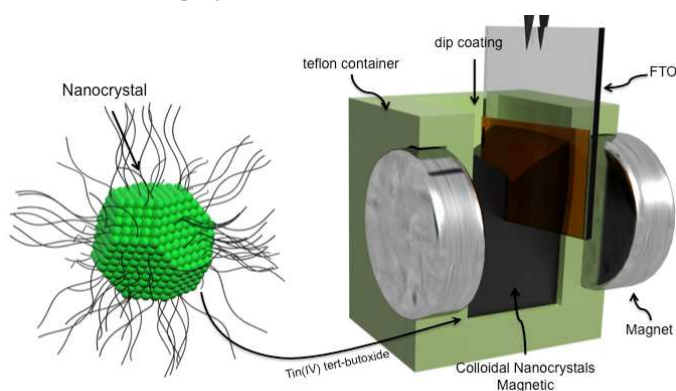
Scheme 1. Magnetic field-assisted dip coating process to produce hematite thin films on the FTO substrate.

Scheme 1 illustrates the magnetic field-assisted dip coating process to produce hematite thin films on the FTO substrate. The maghemite colloidal nanocrystal solution is stored in a Teflon container designed to externally couple two parallel magnets (see

Figure S1, ESI). A similar strategy was used to process the doped hematite photoanode; however, intentional doping was performed by the addition of a specific amount of tin (IV) tert-butoxide as a tin precursor which was chosen due to it solubility in toluene and because it is halogen-free. Experimental details concerning maghemite and deposition processes are available in the ESI†. Figure S2 (see ESI†) is a demonstrative picture of a hematite photoanode deposited on a large substrate of FTO using magnetic field-assisted CND.

During the development of doped and undoped hematite photoanodes prepared by the CND process, we evaluated the influence of the magnetic field using a photocurrent density at 1.23 V_{RHE} (J@1.23 V_{RHE}) as a figure of merit. Note that a single deposition layer was used to avoid several rounds of dip coating and sintering steps. The influence of the magnetic field on the undoped and Sn-doped hematite photoanode performance (assessed by the J at1.23V_{RHE}) and nanostructure are summarized in Table I. The use of magnetic field during the dip-coating process produces an increase in the photocurrent and the film thickness. Note that photoanodes processed by multiple deposition steps without the application of a magnetic field did not demonstrate a better photoelectrochemical performance for water splitting (see Figure S3, ESI). We believe the influence of the magnetic field on the CND process is associated with the γ-Fe_2O_3 colloidal dispersion magnetorheological (MR) fluid behavior employed in this study (see Figure S4, ESI). MR fluids are materials, which show a reversible transition from a liquid to a nearly solid state under the presence of external magnetic fields. In the absence of a magnetic field, MR fluids behave as Newtonian fluids. Furthermore, when a magnetic field is applied (transverse to the direction of flow) a yielding, shear thinning and viscoelastic behavior is observed.[17] These modifications, which are induced by the magnetic field in the γ-Fe_2O_3 colloidal dispersion rheological behavior have a direct impact on the dip-coating process and facilitate the preparation of films with thicknesses ranging from 150-250 nm, in a single step (see Figure S5, on the ESI).

Table I – Influence of the magnetic field applied during the dip-coating process on the photocurrent density at 1.23 V_{RHE} and thin film thickness of undoped and Sn-doped hematite photoanodes.

α-Fe_2O_3 Photoanode	with magnetic field		without magnetic field	
	undoped	Sn-doped	undoped	Sn-doped
Thickness (nm)(#)	180	250	91	99
J @1.23V_{RHE} (mA/cm^2)	1.4	2.7	1.0	1.1

(*) Samples sintered at 850°C; (#) measured by cross sectional FE-SEM images

Henceforth, all results reported in this communication are related to photoanodes prepared by the CND process with magnetic field applied during the dip-coating process. First, we optimized the sintering process for the undoped hematite thin film in different ranges of temperatures and times. Figure S6 (see ESI†) displays the photocurrent density as a function of the sintering time for undoped hematite sintered at 800 °C and 850 °C. This temperature range was chosen because below 800 °C a very low photocurrent is observed; the reproducibility is affected drastically above 850 °C due to uncontrollable grain growth or substrate damage. For undoped hematite, the best photoresponse was obtained at 850 °C with a soaking time of 20 min. At these sintering parameters, a photocurrent of 1.4 mA.cm^{-2} at 1.23 V_{RHE} and a plateau of 1.9 mA.cm^{-2} at 1.5 V_{RHE} were achieved under standard AM 1.5 G

illumination (see the current potential curve in Figure 1a). In our previous study,[16a] we reported a photocurrent value of 1.1 mA.cm^{-2} at 1.23 V_{RHE} for a film formed by six layers of hematite with a thickness higher then 900 nm. Modifications implemented in the CND process (i.e., the magnetic field and the use of maghemite) produced a highly oriented film which was formed by a single layer of hematite with a 27% improved photocurrent.
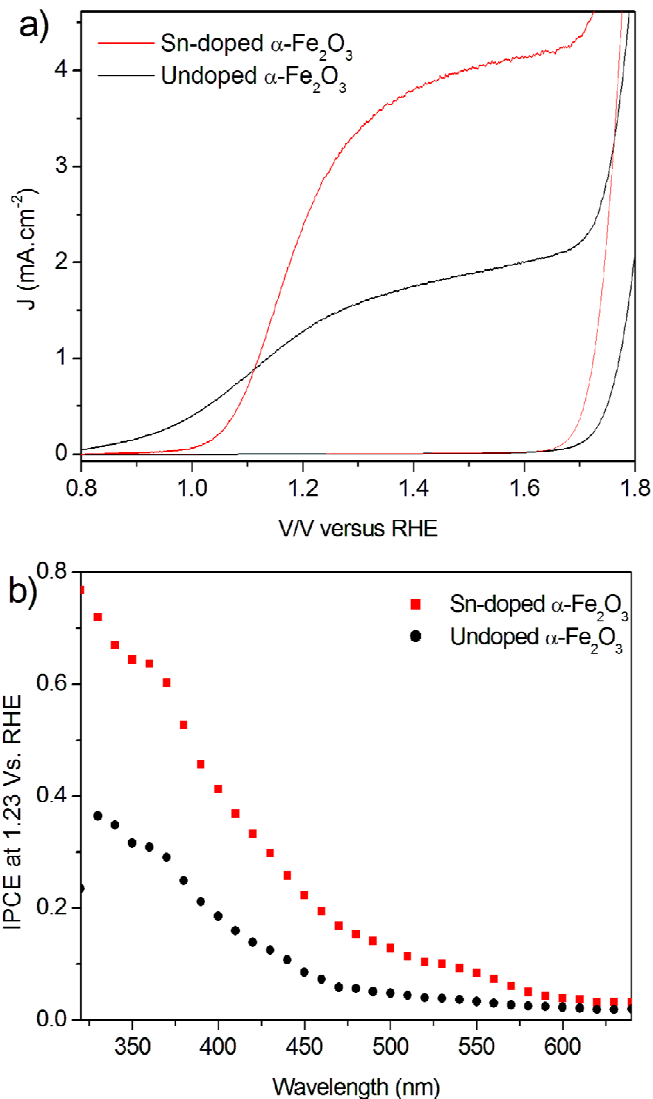
Figure 1. Photoelectrochemical analysis of a hematite photoanode prepared by CND. (a) Current density potential curve for Sn-doped hematite (red line – sintered at 850°C/3 min.) and undoped hematite (black line – sintered at 850°C/20 min.) under simulated solar light and dark conditions; (b) Incident photon-to-current efficiency (IPCE) plots versus wavelength for Sn-doped hematite (diamond markers) and undoped hematite (circle markers); the IPCE was measured at 1.23 V_{RHE}.

The X-ray diffraction (XRD) analysis performed on the film after the sintering process shows the formation of a hematite phase with preferential orientation along the [110] axis vertical to the substrate (see Figure S7, ESI†). Figures 2a,c illustrate top view and cross-sectional analyses of the undoped hematite film which was

characterized by field emission scanning electron microscopy (FE-SEM). The top view analysis (see Figure 2a) shows the nanostructured nature of the film with elongated grains (with the smallest feature size in the range of 75 nm) and open porosity. The cross-sectional analysis (see Figure 2c) shows a film formed by columnar grains with a thickness of 180 nm; note that a single column of hematite grains forms the film. The cross-sectional analysis by transmission electron microscopy (TEM) and high-resolution transmission electron microscopy (HRTEM) (see Figure S8, ESI†) confirm the formation of columnar grains with a good interface between the hematite and FTO and the coherent grain boundary between hematite grains (see Figures S5b,c, ESI†). FE-SEM and TEM/HRTEM analyses of the undoped film reveal an unexpected nanostructural evolution after the sintering process. These observations generated *in-situ* TEM experiments using a sample holder with a hot-stage which was conducted at 850 °C. The undoped colloidal maghemite was deposited on an amorphous silicon nitride membrane (thickness of 10 nm) and pretreated at 450 °C in a rapid thermal annealing furnace to promote the burn-out of the organic layer and promote the transformation to hematite. The video of the *in-situ* experiment and TEM images (see Figure S9, ESI† and video) clearly show that the orientation process occurs via a grain boundary motion without the grain rotation. The contrast in the difference between the two grains is related to the crystallographic orientation; after the junction of two particles, a clear interface is formed. Also, displacement of the interface in the direction of the smaller grain and the formation of a single grain with the same contrast as the large grain is apparent which indicates that the smaller grain assumes the crystallographic orientation of the larger grain. A similar process must occur during thin film sintering which results in a columnar and textured structure.
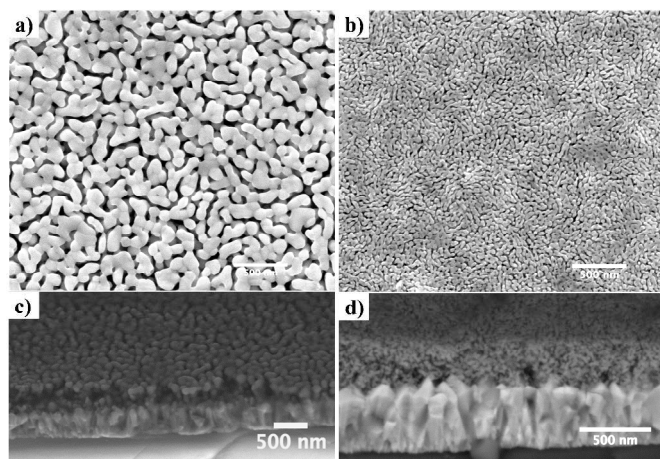

Figure 2. FE-SEM images for hematite thin films obtained by CND. a) Top view image for undoped hematite annealed at 850 °C for 20 min. b) top view image for Sn-doped hematite annealed at 850 °C for 3 min.; c) and d) are cross sectional images for undoped and Sn-doped hematite, respectively. All images are in the same magnification.

As the undoped hematite achieved the best photocurrent value when sintered at 850 °C, we selected this sintering temperature to study the effect of the addition of Sn on the photoelectrochemical performance of the hematite photoanode prepared by using the CND process. At this stage, we also evaluated the optimum concentration of Sn precursor in relation to the concentration of maghemite nanocrystals; the best concentration was 8% of precursor in relation to the maghemite mass. As illustrated in Figure 1a, the photocurrent
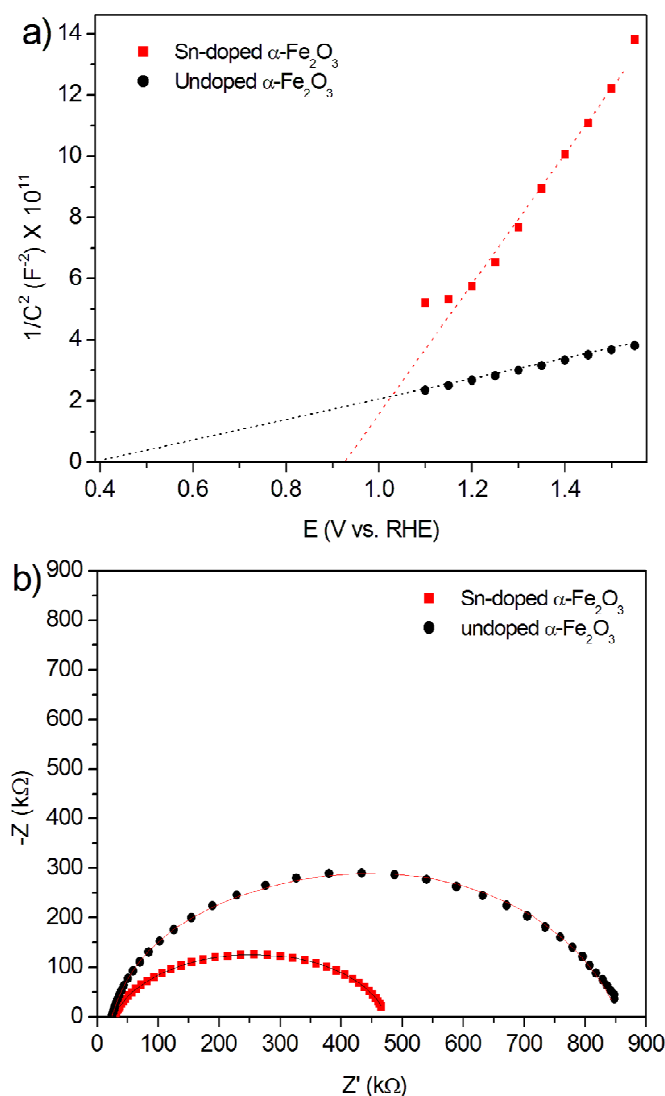
achieved a value of 2.7 mA.cm^{-2} at 1.23 $_{VRHE}$ and reached a plateau of 3.8 mA.cm^{-2} at 1.5 V$_{RHE}$ for the Sn-doped hematite thin film. The photocurrent at 1.23 V$_{RHE}$ of the Sn-doped sample increased by 93% as compared to the undoped sample. Note that this value is comparable or even higher than the best photocurrent values reported for hematite without a catalyst which was prepared by using the APCVD process or the hydrothermal method.[12,15] In addition, the Sn-doped hematite chrono-amperometry measurement showed excellent stability (see Figure S10, ESI†).

IPCEs were realized for both Sn-doped doped and undoped photoanodes at 1.23 V$_{RHE}$. An IPCE value of 78% at 320 nm and 40% at 400 nm was observed for Sn-doped hematite thin films (see Figure 1b - red square); IPCEs of 39% at 320 nm and 20% at 400 nm were measured for undoped hematite (black dot) which validates the higher value of IPCE in the wavelength range analyzed for doped hematite as compared to the undoped material. Integrating the overlap of IPCE data measured at 1.23 V$_{RHE}$ with the standard AM1.5/100 mW.cm^{-2} solar spectrum gives calculated photocurrent values of 2.6 mA.cm^{-2} and 1.3 mA.cm^{-2} for Sn-doped hematite and undoped hematite, respectively, which are similar to values measured by the current-potential curve and confirms that the employed light source simulated the AM1.5 solar emission.

The XRD analysis of the Sn-doped film after the sintering process reveals the formation of a hematite phase with no traces of the undesired phase. As observed in the undoped film, this sample also showed preferential orientation along the [110] axis vertical to the substrate (see Figure S7, ESI†). Crystallite sizes, which were calculated by the Scherrer equation, for undoped and doped hematite were 78 nm and 41 nm, respectively. The FE-SEM analysis (see Figure 2 c-d) supports the XRD analysis and shows an impressive decrease in the grain size with the addition of Sn. These results strongly suggest that during the sintering process, Sn^{+4} segregation occurs along solid-solid and solid-gas surfaces which hinders the grain growth process.[15,18] The cation segregation can promote either a decrease in the grain boundary mobility or a surface energy reduction. Both phenomena will contribute to a decrease in the grain growth rate.[18-21] The segregation phenomenon was investigated by scanning transmission electron microscopy (STEM) with X-ray energy dispersive analysis (EDS) in the film cross-section. As illustrated in Figure S11, ESI†, the line profile EDS analysis along the hematite grain showed an Sn enrichment in the grain surface which confirms the segregation process. Note that the undoped sample did not show any sign of impurities (see the STEM-EDS analysis in Figure S11, ESI†). The cross-sectional analysis performed by STEM and FE-SEM (see Figure 2d) shows a mesoporous film formed by elongated grains with a thickness of 250 nm. Note that after the Sn addition, the columnar structure disappears.

To obtain a better understanding of the effect of the Sn addition on the photoelectrochemistry of the doped hematite photoanode, electrochemical impedance spectroscopy (see details in Figure S12 and Table S1, ESI) and a Mott-Schottky analysis was performed to estimate the donor density (N$_D$) and the flat band potential (V$_{fb}$). Figure 3a displays the Mott-Schottky plot for doped and undoped hematite thin films recorded in the absence of light. A good linear fit (with a R^2 > 0.99 for both samples) was obtained in the bias range from 0.9 to 1.4 V$_{RHE}$ with a positive slope, which is typical of an n-type semiconductor. N$_D$ and V$_{fb}$ values measured for both films are listed in Table S2. The N$_D$ value analysis was unchanged and corresponds to 1.3x10^{18} cm^{-3} and 1.7x10^{18} cm^{-3} for undoped and Sn-doped photoanodes, respectively. This result suggests that Sn does

not act as an electronic dopant. In contrast, clearly the addition of Sn promotes a significant anodic shift of the V_{fb} in relation to the undoped film. The increase in the V_{fb} must be associated with Sn enrichment in the hematite grain surface. The increase of the V_{fb} promotes an increase in band-bending which can contribute to the charge separation process.[22]

a smaller diameter when compared to an undoped hematite anode which indicates a smaller charge transference resistance. These results suggest that the Sn segregation layer in the hematite surface facilitates the charge transference at the semiconductor-liquid junction. The exact effect of Sn segregation in the charge transference is unknown. However, clearly the association of a smaller charge transference resistance with a higher surface area contributes to a superior photoelectrochemical performance for water splitting of the doped photoanode.

Conclusions

In conclusion, we improved the CND process by using the deposition of maghemite (γ-Fe$_2$O$_3$) nanocrystals and by introducing the magnetic field during the dip coating process to improve the thin film deposition method, which is mainly due to the MR fluid behavior of this colloid. These modifications produced a highly oriented and transparent thin film formed by a single layer of hematite (thickness ~180 nm) with a photocurrent of 1.4 mA.cm^{-2} at 1.23 V_{RHE}. We also introduced an intentional dopant and added a Sn precursor during the deposition process. The photocurrent achieved for the doped photoanode was 2.7 mA.cm^{-2} at 1.23 V_{RHE}. The improvement in the photocurrent is attributed to an increase in band-bending and to a smaller charge transference resistance associated with a higher surface area; this behavior is facilitated by the addition of Sn.

Acknowledgements

Notes and references

Department of Chemistry, Federal University of Sao Carlos, 13565-905 Sao Carlos, SP, Brazil

Corresponding Author

edson.leite@pq.cnpq.br

Figure 3. a) Mott-Schottky plots measured at 1kHz for Sn-doped and undoped hematite photoanodes. The flat-band potential is determined on the linear fit slope intercept for both curves; b) Nyquist plot of the electrochemical impedance spectroscopy analysis for Sn-doped and undoped hematite thin films measured at 1.75 V_{RHE}.

In addition, defining the pseudo-overpotential for water oxidation (η_{OX}) as the difference between the onset voltage for a photocurrent (V_{on}) under standard illumination conditions and the V_{fb} i.e., $\eta_{OX} = (V_{on} - V_{fb})$,[23] there is a small value of η_{OX} (0.1 V) for the doped photoanode as compared to the undoped film (0.4 V). We therefore performed a simple qualitative electrochemical impedance spectroscopy analysis to determine the effect of the addition of Sn on the η_{OX}. The Sn-doped anode Nyquist plot showed a semicircle with

1   K. L. Hardee and A. J. Bard, *J. Electrochem. Soc.* 1976, **123**, 1024−1026.
2   K. Itoh, and J. O. Bockris, *J. Electrochem. Soc.* 1984, 131, 1266.
3   F. Morin, *J. Electrochem. Soc.* 1978, **125**, 709.
4   M.P. Dare-Edwards, J.B. Goodenough, A. Hamnett and P.R. Trevellick, *J. Chem. Soc., Faraday Trans.* 1983, **79**, 2027-2041.
5   C. Gleitzer, J. Nowotny and M. Rekas, *Applied Physics A*, 1991, **53**, 4, 310-316.
6   D.S. Tilley, M. Cornuz, K. Sivula and M. Gratzel, *Angew. Chem., Int. Ed.* 2010, **49**, 1−5.
7   K. Sivula, R. Zboril, F.L. Formal, R. Robert, A. Weidenkaff, J. Tucek, J. Frydrych and M. Gratzel, *J. Am. Chem. Soc.* 2010, **132**, 7436− 7444.
8   B. M. Klahr, A. B. F. Martinson and T. W. Hamann, *Langmuir* 2011, **27**, 461−468.
9   F. Le Formal, M. Graetzel and K. Sivula, *Adv. Funct. Mater.* 2010, **20** 1099−1107.

10 L. Li, Y. Yu, F. Meng, Y. Tan, R. J. Hamers and S. Jin, *Nano Lett.* 2012, **12**, 724-731.

11 S. C. Warren, K. Voitchovsky, H. Dotan, C.M.. Leroy, M. Cornuz, F. Stellacci, C. Hebert, A. Rothschild and M. Gratzel, *Nature Materials,* 2013, **12**, 842–849.

12 A. Kay, I. Cesar and M. Grätzel, *J. Am. Chem. Soc.,* 2006, **128**, 49, 15714–15721.

13   a) N. T. Hahn, H. Ye, D. W. Flaherty, A. J. Bard and C. B. Mullins, *ACS Nano*, 2010, **4**, 1977. b) O. Zandi, B.M. Klahr and T. W. Hamann, *Energy Environ. Sci.,* 2013, **6**, 634-642.

14 Y. Lin, S. Zhou, W. S. Sheehan, D. Wang, *J. Am. Chem. Soc.,* 2011, **133** (8), 2398–2401.

15   L. Xi, Y. S. Chiam, F. W. Mak, D. P.; Tran Barber, J.; Loo C. J. S.; Wong H. L. *Chem. Sci.,* 2013,4, 164-169.

16   a) R.H. Goncalves, B. H. R. Lima and E. R. Leite, *J. Am. Chem. Soc.*, 2011, **133** (15),6012–6019; b) R.H. Gonçalves, L. D. T. Leite, E. R. Leite *ChemSusChem* 2012, **5** , (12), 2341-2347. c) A.N.; Pinheiro, E. G. S. Firmiano, A. C. Rabelo, C. J. Dalmaschio, E. R. Leite *RSC Adv.,* 2014, **4**, 2029.

17 J. Vicente, D. J. Klingenberg, R. Hidalgo-Alvarez, *Soft Matter*, 2011, **7**, 3701-3710.

18 G. Carbajal-Franco, A. Avila-Garcia, A. Tiburcio-Silver, D. Gouvea, R.H.R. Castro, *J. of Nanosci. and Nanotechnol.* 2010, **10**, 1338-1342.

19 I. Cesar, K. Sivula, A. Kay, R. Zboril and M. Graetzel, *Journal Of Physical Chemistry C*, 2009, **113**, 772-782.

20   E. R. Leite, A. P. Maciel, I. T. Weber, P. N. Lisboa-Filho, E. Longo, C. O. Paiva-Santos, A. V. C. Andrade, C. A. Paskocimas, Y. Maniette, W. H. Schreiner, *Adv. Mater.* 2002, 14, 905.

21 Chiang, Y-M; Dimie lll, D.; Kingery, W.D.; *Physical Ceramics Principle for Cerimic Science and Engineering*, **1997**, Jonh Wiley, New York.

22 M. Barroso, C. A. Mesa, S. R. Pendlebury, A. J. Cowan, T. Hisatomi, K. Sivula, M. Grätzel, D. R. Klug and J. R. Durrant, *Proc. Natl. Acad. Sci.* 2012, 109, 39, 15640-15645.

23   K. Sivula, *Journal Of Physical Chemistry Letters.* 2013, 4, 10, 1624-1633.
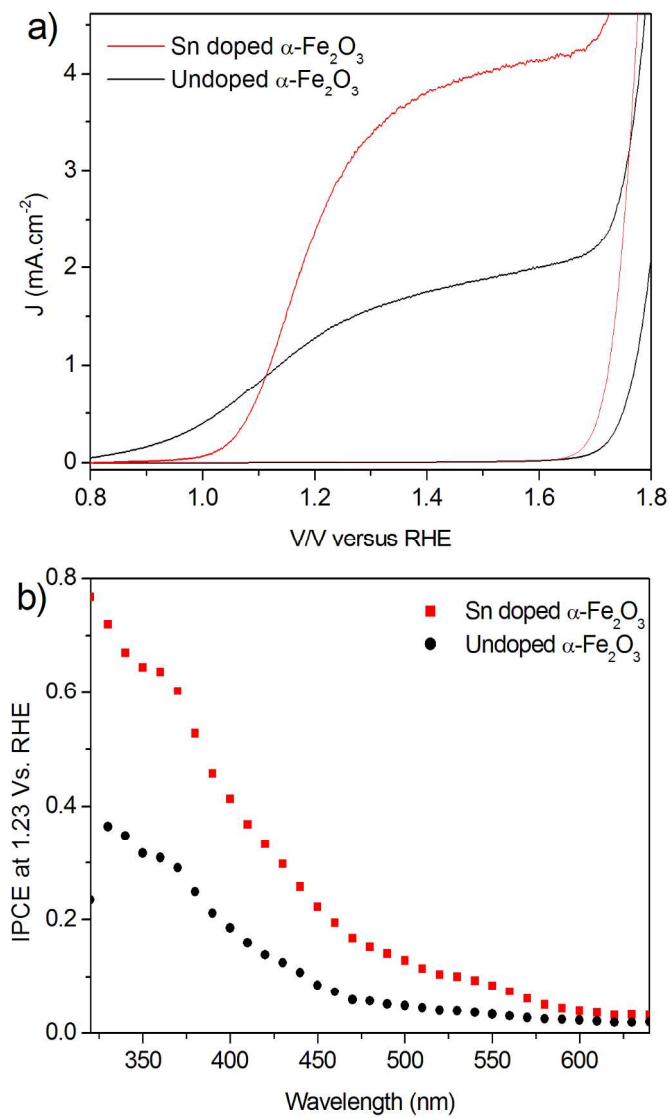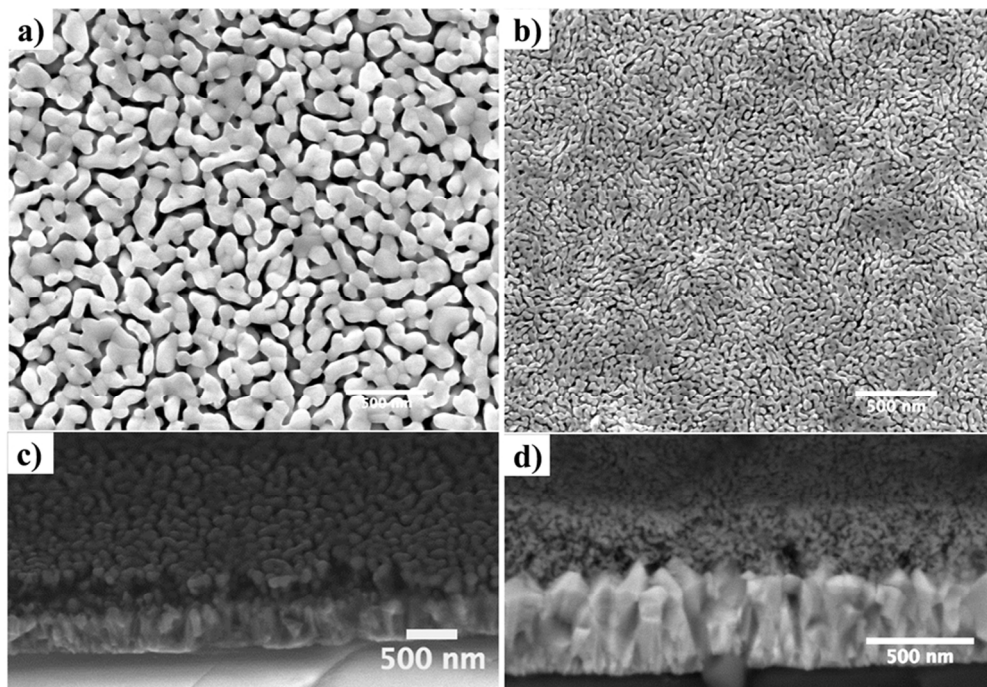
Figure 1
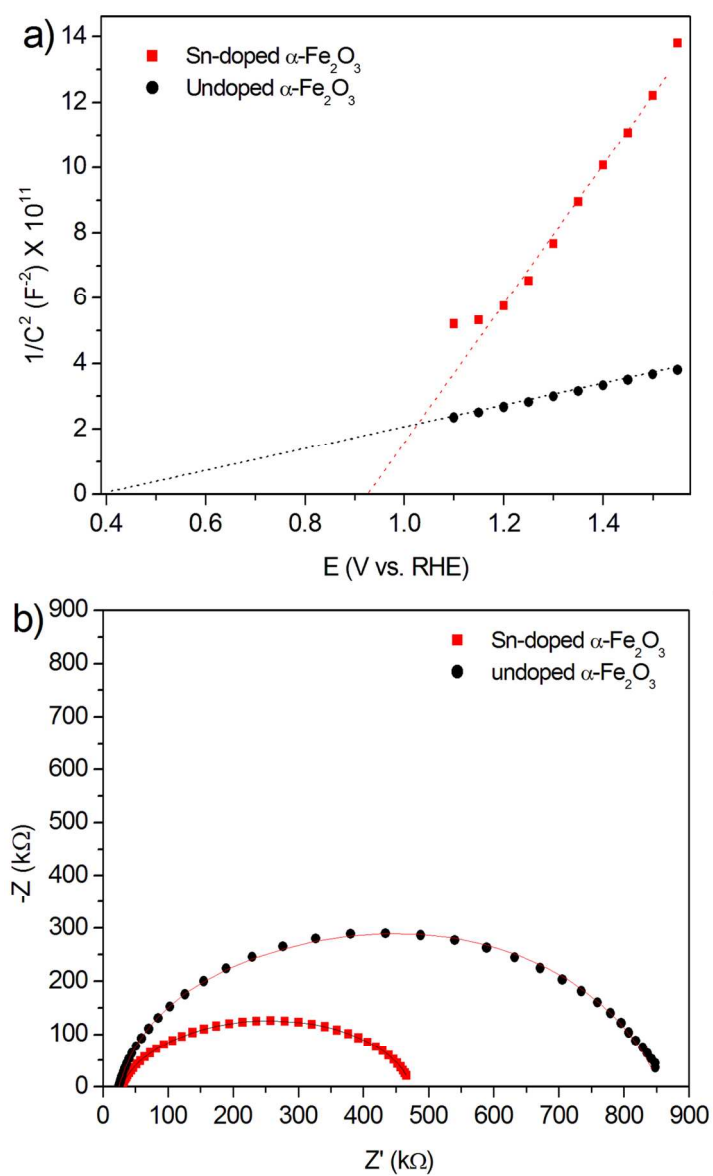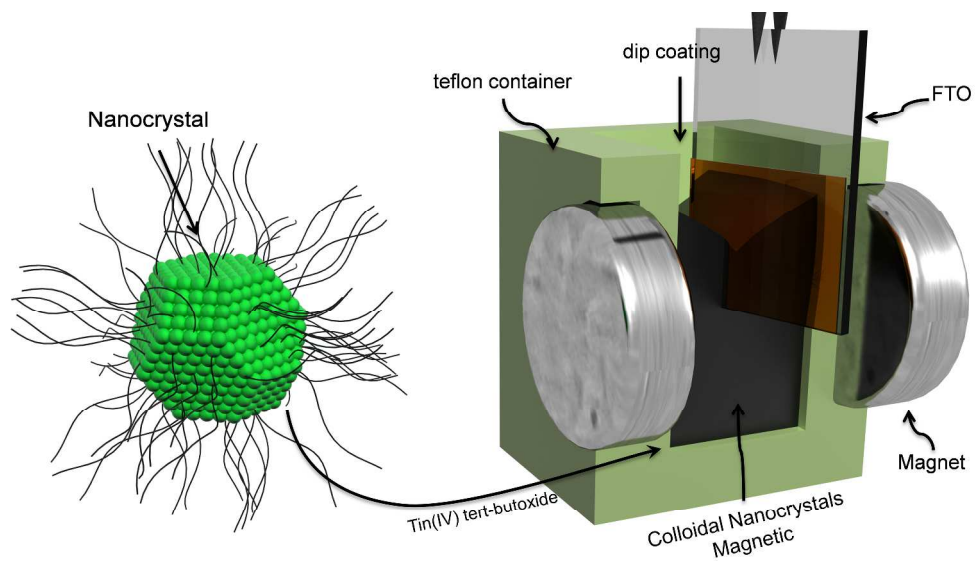670x1188mm (96 x 96 DPI)

Figure2
270x187mm (96 x 96 DPI)

Figure 3
203x343mm (150 x 150 DPI)

Scheme1
1527x910mm (96 x 96 DPI)

Broader Context

An excellent and potentially efficient route to storing solar energy is to convert light into chemical energy in the form of chemical bonds, which is a form of artificial photosynthesis. Considering the abundance of H_2O on the planet, water splitting is a natural pathway for artificial photosynthesis. Hematite is an n-type semiconductor with high chemical and photoelectrochemical stability. This oxide is considered the most promising material to be used as a photoanode for water splitting. In this study, we demonstrate a significant advance in the colloidal nanocrystal deposition process to obtain hematite thin films with a high photoelectrochemical performance. We introduced the following modifications in the original process: a) the deposition of maghemite (γ-Fe_2O_3) instead of magnetite; b) the introduction of a magnetic field during the dip coating process; and c) the introduction of intentional doping. Using this non-aqueous deposition route, we produced undoped and Sn-doped hematite photoanodes with excellent photocurrents of 1.5 mA.cm^{-2} at 1.23 V_{RHE} and 2.7 mA.cm^{-2} at 1.23 V_{RHE}, respectively, under a standard AM1.5G solar light simulator. The association of colloidal deposition of MR fluid in the presence of an external magnetic field with a sintering process facilitates the attainment of textured columnar or mesoporous thin film morphologies. The intentional addition of a doping element promotes a significant modification in the thin film morphology and demonstrates that the present deposition process is quite versatile. Furthermore, the thin film deposition process described in this study showcases their promising potential applications in different fields that demand porous thin films such as sensors, batteries, fuel cells and solar cells.